1
Synthesis, Assembly, and Applications of Semiconductor Nanomembranes

Zheng Yan, Kewang Nan, and John A. Rogers

1.1
Introduction

The origins of nanoscience and nanotechnology can be traced in large part, at least from the standpoint of material sciences, to seminal research on cadmium selenide nanocrystals [1] and spherical fullerenes [2]. Studies of these and other related zero-dimensional (0D) materials soon expanded to one-dimensional (1D) nanostructures, such as nanowires and nanotubes [3–5]. Although such 1D nanostructures are comparatively easy to manipulate and to interface with contact metallization, building general classes of semiconductor devices at interesting levels of integration with individual wires and tubes is challenging, perhaps prohibitively so, due to lack of means for uniform synthesis and assembly. More recent activities in electronic nanomaterials explore, as an alternative, ultrathin membranes or two-dimensional (2D) layers of semiconductors, sometimes referred to generically as semiconductor nanomembranes (NMs) [6–14]. The 2D, planar geometries facilitate integration into device systems with realistic pathways to manufacturing; they also afford easy formation of electrical contacts and natural compatibility with well-developed thin-film growth and processing technologies.

Many classes of advanced materials can be physically isolated or chemically synthesized in the form of NMs, including organics such as graphene and 2D polymers, and inorganics such as silicon, germanium, gallium arsenide (GaAs), gallium nitride, and transition-metal dichalcogenides [6–14]. Existing transfer-printing approaches allow the manipulation of NMs with thicknesses down to the atomic level and with lateral dimensions of up to dozens of inches [7, 11–13]. Recent research efforts establish strategies for deforming NMs into complex, three-dimensional (3D) configurations, conforming them onto tissue-like curvilinear surfaces, and deterministic assembly of them onto substrates of interest with high fidelity in positions and orientations [12, 13]. Many NM-based advanced functional device systems have been realized, demonstrating high operating performance, unique stretchability and flexibility, 3D layouts, physical disappearance at programmed rates, and many other attractive

Silicon Nanomembranes: Fundamental Science and Applications, First Edition.
Edited by John A. Rogers and Jong-Hyun Ahn.
© 2016 Wiley-VCH Verlag GmbH & Co. KGaA. Published 2016 by Wiley-VCH Verlag GmbH & Co. KGaA.

features, which are hardly achievable in their related bulk counterparts, or with 0D and 1D nanomaterials [12, 13].

Single-crystal silicon NMs are particularly appealing because of capabilities in high-quality synthesis over large areas and with precise thicknesses at relatively low cost in the nanometer regime; they are also naturally compatible with conventional fabrication techniques and can be fully exploited in unique, high-performance electronic, and optoelectronic systems [12, 13]. In addition, the nanoscale thicknesses of silicon NMs enable many attractive features, which are unavailable in their bulk counterparts, such as high flexibility due to the linear decrease of bending strains with thicknesses, fast dissolution in biofluids because of their nanoscale geometries, splitting of the conduction band valleys induced by electronic confinement effects, and manipulation of heat flow allowed by phonon confinement effects [13]. The following sections describe recent research advancements in silicon NMs including synthesis, assembly, and device integration.

1.2 Strategies for Forming Silicon Nanomembranes

Development of methods to synthesize high-quality silicon NMs with precise thicknesses and lateral dimensions is crucial for creating high-performance, reliable electronic devices. An attractive approach is to exploit single-crystal silicon wafers, which are already well-developed commodity items that have exceptional levels of purity and doping control, with smooth surfaces and high carrier mobilities. Thus, silicon NMs isolated from wafers naturally adopt similarly high material quality, to enable high-performance electronic and optoelectronic devices. The following sections highlight two strategies that exploit wet-chemical etching techniques and conventional lithographic processing.

1.2.1 Selective Etching to Release Nanomembranes from Layered Assemblies

The most straightforward approach involves the selective etching of buried sacrificial layers from multilayered silicon wafers [11–14]. As shown in the scheme of Figure 1.1a, the selective removal of silicon dioxide (SiO_2) from a silicon-on-insulator (SOI) wafer by immersion in hydrofluoric acid (HF) releases the top silicon layer as an NM. The optical image on the right shows a silicon NM (~50 nm in thickness) formed in this manner. After transfer onto a new host, the wrinkles on silicon NMs can flatten [13] or they can be used to advantage in stretchable electronics, as described subsequently. NMs with thicknesses as small as 20 nm can be synthesized directly from commercially available SOI wafers. Further reductions in thickness to values down to ~2 nm are possible via multiple cycles of thermal oxidation followed by HF etching [17]. Patterning steps based on conventional photolithography and electron beam lithography or on soft lithography and

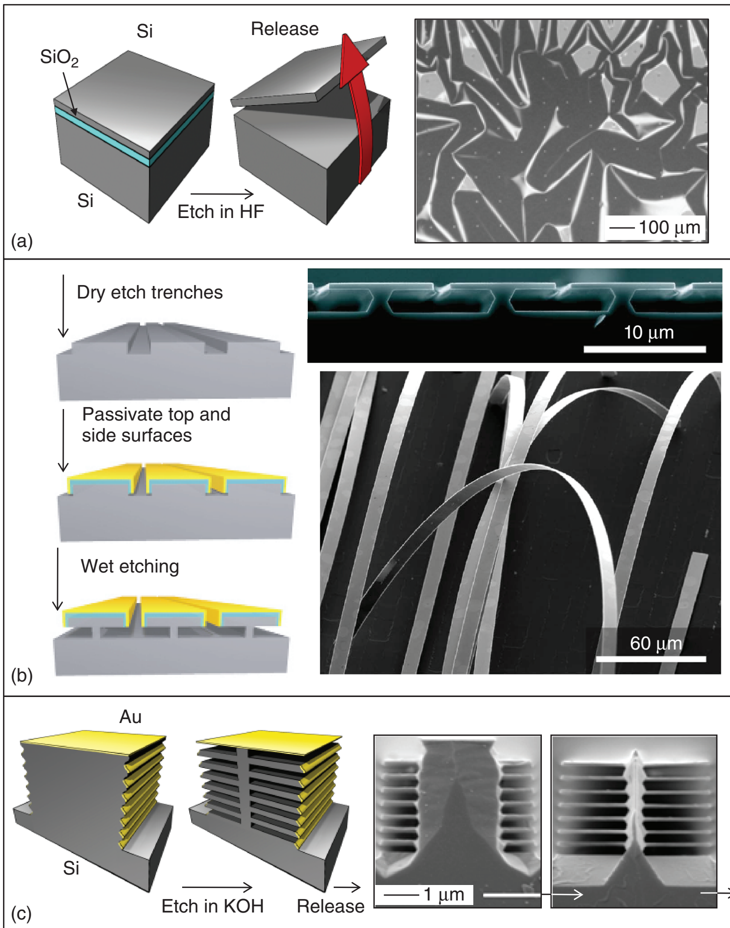

Figure 1.1 Representative routes for making single-crystal silicon NMs. (a) Release of a silicon NM from an SOI wafer by selective removal of SiO_2 in hydrofluoric acid. The optical image on right shows a single-crystal silicon NM (~50 nm in thickness) formed by this manner. After transfer onto a new host, the wrinkles in the silicon NM can flatten. (Reproduced from Rogers *et al.* [13], with permission of Nature Publishing.) (b) Fabrication of silicon NMs by anisotropic wet-chemistry etching of bulk silicon (111) wafers. The frame on the top right is an SEM image of partially undercut silicon NMs. The frame on the bottom right is an SEM image of released silicon NMs. Left frame: Reproduced from Baca *et al.* [15], with permission of Wiley. Right frame: Reproduced from Mack *et al.* [16], with permission of AIP. (c) Generating multilayer stacks of silicon NMs from bulk silicon (111) wafers by anisotropic etching. The processes exploit trenches with sculpted sidewalls, angled electron beam evaporation of gold, and anisotropic wet chemical etching. The cross-sectional SEM images on the right show two intermediate stages of forming stacks of silicon NMs (~100 nm in thickness) in this manner. (Reproduced from Rogers *et al.* [13], with permission of Nature Publishing.)

nanoimprint lithography can yield wide ranging geometries and spatial layouts of silicon NMs created in this way [12]. With careful control, lateral dimensions down to ~17 nm are possible [12].

Other semiconductor NMs can also be released from other layered assemblies on wafers, such as stacks of GaAs separated by aluminum gallium arsenide (AlGaAs), germanium (Ge), or silicon-germanium (SiGe) on insulators, and many other III–V semiconductors and their combinations [12, 13, 18, 19]. Moreover, nanotubes or other unusual structures can be fabricated when certain constituent layers are grown/deposited with controlled levels of residual stress [20–22]. The diameters of tubes created in this way follow from the thicknesses of the layers and their stresses [20].

1.2.2
Anisotropic Etching to Release Silicon Nanomembranes from Bulk Silicon Wafers

Although release of silicon NMs from SOI wafers is simple, the high cost of such substrates can be a drawback for certain applications. Anisotropic etching along certain crystalline planes provides an alternative, capable of generating large quantities of silicon NMs from bulk silicon wafers at low cost [12, 13, 15, 16, 23].

Figure 1.1b depicts the fabrication procedures, starting with bulk silicon (111) wafers [16]. The first step involves defining trenches perpendicular to the (110) plane by photolithography and reactive ion etching (RIE). Depositing SiO_2, Si_3N_4, and Au, in sequence, passivates the top surfaces and side walls of the resulting wafer. Anisotropic etching induced by immersion in a solution of potassium hydroxide (KOH), an etchant that shows high etching selectivity along the (110) planes, yields high-quality silicon NMs. Appropriate control of etching parameters enables thicknesses of NMs between several tens and several hundreds of nanometers. The initial photolithography step defines the lateral dimensions, from tens of nanometers to the sizes of entire wafers. The top right of Figure 1.1b presents a scanning electron microscope (SEM) image of partially undercut silicon NMs; the bottom right shows similar structures after complete undercut. As-fabricated NMs have surface roughness of ~0.5 nm, as measured by atomic force microscopy (AFM) [12]. The major drawback of KOH is that mobile ions introduced during the etching process can be detrimental to electronic applications. Consequently, CMOS-compatible wet etchants, such as tetramethylammonium hydroxide (TMAH), are preferred [15].

Large quantities of silicon NMs can be generated either by repeated application of the aforementioned procedures or by alternative techniques illustrated in Figure 1.1c. Such a strategy combines trenches with sculpted sidewalls, angled electron beam evaporation of gold resists, and anisotropic wet chemical etching using KOH [23]. The first step defines trenches on the bulk silicon wafers with (111) orientations, as before. The trench etching then proceeds using an inductively coupled plasma-RIE etching process that sculpts ripples, with engineering control, onto the side walls. Depositing gold at an angle onto these ripples yields isolated strips that serve as masks for anisotropic etching along the (110)

directions by KOH. The cross-sectional SEM images on the right of Figure 1.1c show two intermediate stages of making stacked silicon NMs (~100 nm in thickness) in this manner. Bulk-like quantities of silicon NMs can then be released for integration into devices.

As with the SOI based approach, this scheme enables precisely controlled dimensions, crystallinity, and doping levels of the silicon NMs. Lithographically defined lateral dimensions and spatial positions render them naturally compatible with strategies of deterministic assembly based on transfer printing for heterogeneous integration and approaches in compressive buckling for stretchable devices, as described in the following sections.

1.3 Transfer Printing for Deterministic Assembly

1.3.1 Introduction

A general challenge for integrating fragile building elements of silicon NMs into functional devices lies in guiding them into well-defined layouts with extreme accuracy in position and orientation, and high throughput. Transfer printing with soft, elastomeric stamps is the most well-developed approach, which allows the precise, nondestructive manipulation of silicon NMs for the assembly onto diverse substrates of interest [24–33]. Transfer printing maintains mechanical contact to the silicon NMs throughout the process, and is therefore deterministic, enabling high-transfer yields and minimal levels of positional/directional disorders.

Figure 1.2a outlines the transfer printing strategy for silicon NMs [30]. To begin, a soft elastomeric stamp brought into physical contact with silicon NMs forms a robust adhesive interface based on van der Waals interactions (step i). These NMs, regarded as “inks” on a “donor” substrate, result from processes like those described in Figure 1.1, and serve as basic building blocks for semiconductor devices. The stamp may contact all NMs (e.g., using a flat stamp) or a selected fraction of them determined by the spatial features of relief on the surface of the stamp [29]. Peeling the stamp away from the donor at a high rate lifts the NMs onto the surface of the stamp (step ii). The stamp, “inked” in this manner, is then contacted with a receiving substrate (step iii). Slow removal of the stamp ensures high yield “printing,” or transfer, of the NMs from the surface of the stamp to the receiving substrate (step iv). This approach allows integration of silicon NMs onto nearly any type of substrate, and is fully compatible with device grade silicon derived from wafer-scale sources of material. A key feature of this process is that it separates the conditions for growth (e.g., high temperature) from the constraints associated with the final device substrate (e.g., low glass-transition temperature plastics or elastomers).

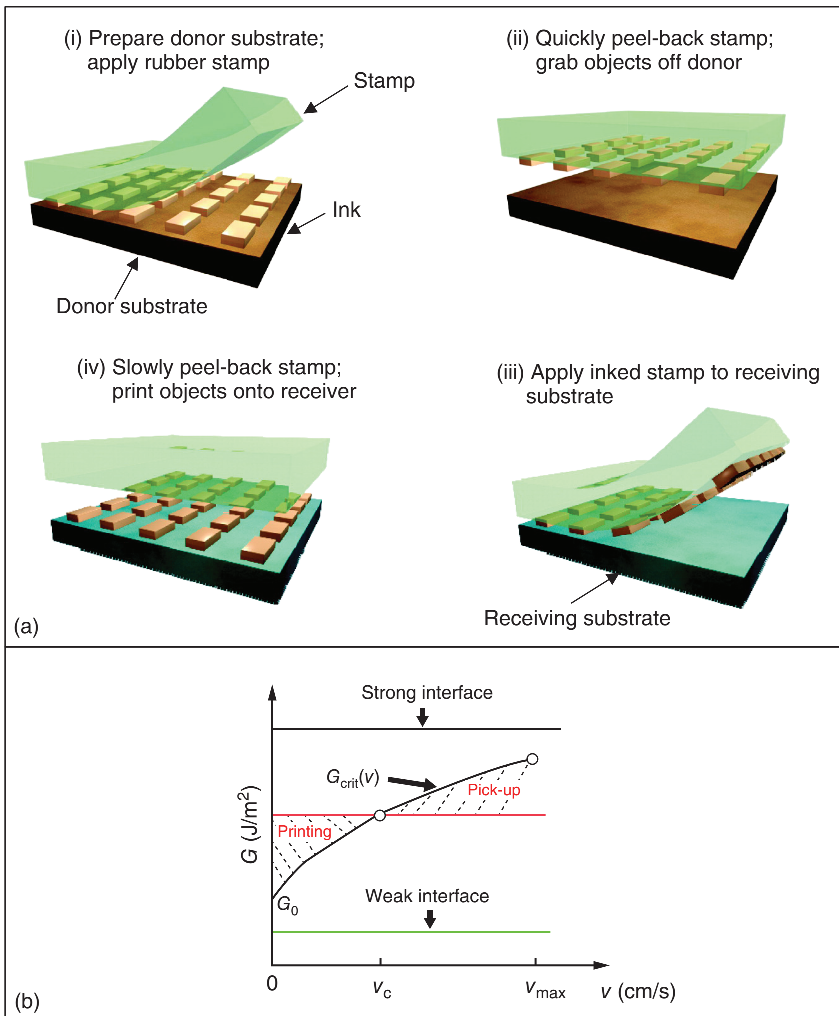

Figure 1.2 (a) Schematic illustration of the process for a transfer-printing approach that uses a rubber stamp to retrieve solid nano-/microstructures of silicon NMs, which can be regarded as "inks," and to deliver them onto device substrates, as a form of deterministic materials assembly. (b) Schematic diagram of critical energy release rates for the ink/receiver interface and for the stamp/ink interface. The horizontal lines at the top and the bottom represent weak and strong ink/receiver interfaces, respectively, corresponding to conditions for which only retrieval or printing can be realized. (Reproduced from Feng *et al.* [30], with permission of American Chemical Society.)

1.3.2 Mechanics of Transfer Printing

Effective transfer relies, fundamentally, on control of adhesion between the ink/donor, the stamp/ink, and the ink/receiver interfaces. The separation/delamination process demonstrated in Figure 1.2a can be regarded as the initiation and propagation of interfacial cracks, viewed as the competing fracture of two interfaces. During the retrieval process of steps (i) and (ii) in Figure 1.2a, release occurs at the ink/donor interface, which must preferentially fail for proper operation of the process. Similarly, printing of inks onto the receiver substrate follows the propagation of cracks at the stamp/ink interface.

Kinetically switchable adhesion is a powerful and widely exploited strategy in transfer printing. This scheme utilizes the viscoelastic nature of soft elastomeric stamps, such as those made of poly(dimethylsioxane) (PDMS) [24, 30]. Here, the adhesive strength changes systematically with velocity of separation of the PDMS stamp from the donor or receiver surface: higher separation velocities yield proportionally stronger adhesion. As a result, a critical separation velocity can be established, above which separation occurs between the ink and the donor substrate (i.e., retrieval) and below which separation occurs between the ink and the stamp (i.e., release). For this purpose, a general steady-state energy release rate G is given by

$$G = F/W \tag{1.1}$$

where W is the width and F is the force applied to the PDMS stamp in the normal direction.

The critical energy release rate for the ink/receiver interface, $G_c^{\text{ink/receiver}}$, is approximately independent of separation velocity due to the insignificant viscoelastic response of the Si NM ink and the receiver [30]. By contrast, the critical energy release rate for the stamp/ink interface, $G_c^{\text{stamp/ink}}(v)$, depends on peeling velocity, v, due to viscoelasticity in the PDMS [30]. Separation either occurs at the stamp/ink or at the ink/receiver interface, respectively, corresponding to $G_c^{\text{stamp/ink}}$ less than or greater than $G_c^{\text{ink/receiver}}$. At a critical separation velocity, v_c, the energy release rates for both interfaces are equal, marking a transition from a retrieval to a printing regime, as shown in Figure 1.2b [30]. For the particular systems described in [24], retrieval and printing occurs efficiently at separation velocities on the order of 10 cm/s or greater, and a few mm/s or less, respectively.

A number of additional concepts can further enhance the efficacy of the transfer-printing approach; these include shear loading methods to give different values of G for the same peeling force [31], engineered stamp surface structures for modulating the contact areas between the stamp and ink [26], pulsed lasers to initiate thermal delamination of the stamp/ink interface [32], and near surface reservoirs and microchannels for tuning of the geometry of interfaces [33]. The first two improvements (i.e., shear loading and surface structures) prove to be particularly valuable. Shear-assisted transfer printing can induce strong

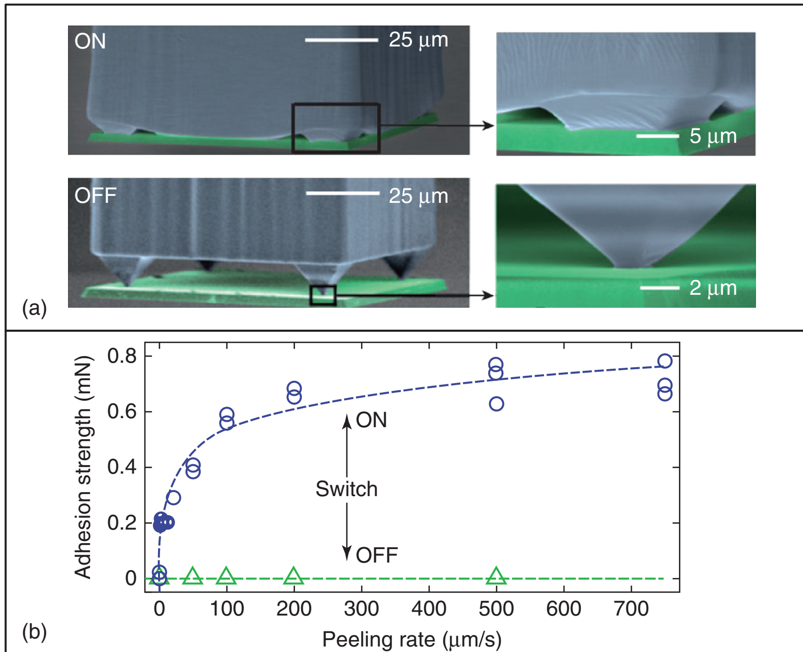

Figure 1.3 (a) Colorized SEM images of elastomeric stamps (blue) bearing soft, pyramidal relief features. Control of the applied pressure provides strong adhesion in a collapsed state (ON, top panel) and weak adhesion in a retracted state (OFF, bottom panel). (b) Measured adhesion strength as a function of peeling velocity in the ON and OFF states. (Reproduced from Kim *et al.* [26], Copyright (2010) National Academy of Sciences, U.S.A.)

interfacial moments between the stamp/ink interface to weaken the adhesion [31]. Increasing the magnitudes of these shear strains improves the efficiency of printing, especially onto challenging (e.g., rough) substrates, by reducing the adhesion of the ink to the stamp to negligible levels. As an advanced example of the use of stamp surface structures, Figure 1.3a shows colorized SEM images of a PMDS stamp (blue) with pyramidal microtips at its four corners. This structure allows pressure-induced modulation of the contact areas, thereby switching between states of strong adhesion (ON) and weak adhesion (OFF), for high-efficiency retrieval and release of silicon NMs (green) [26]. Quantitative data in Figure 1.3b reveal high-contrast switching due to combined geometric and viscoelastic effects [26].

1.3.3
Transfer Printing for Single- and Multilayer Deterministic Assembly

The transfer-printing approaches outlined in Figures 1.2 and 1.3 enable assembly of nano-/microstructured forms of silicon NMs, and many other classes of materials, onto nearly any type of substrate at room temperature and in a rapid, parallel

fashion. Repetitive cycles of printing can yield single- and multilayer assemblies of silicon NMs over small or large areas, with two or three-dimensional layouts and even heterogeneously integrated with other functional materials.

Figure 1.4a shows an example of organized collections of GaAs NMs retrieved from a donor wafer and printed onto a flat glass plate (the main optical image) and a bent plastic substrate (the inset optical image) using repetitive transfer printing as demonstrated in the schematic illustration (the left frame) [34]. This process can create dense or sparse arrays of semiconductor nanomaterials onto target substrates that are even larger than the mother wafer. Another example for the selective transfer and accurate registration appears in the left frame of Figure 1.4b. Here, a pattern of printed silicon NMs form the text “DARPA MacroE” on a flexible polyethylene terephthalate (PET) substrate [25]. The enlarged image of the letter “A” demonstrates the high fidelity of the transfer. As an example of three-dimensional hybrid structures, the right frame in Figure 1.4b shows a cross-sectional SEM image of an eight-layer stack of silicon NMs, each separated by a transparent polymer film [13]. Such structures can be useful in multilayer optoelectronic devices for phase-controlled beam steering. Multilevel flexible electronic devices are also possible, by integrating silicon, gallium nitride, and single-walled carbon nanotubes into three-dimensional heterogeneous structures on polyimide substrates [35]. Recent progress even allows transfer printing of rolled-up NMs [36].

For many simple operations, transfer printing can be manually performed. Precise control can be accomplished with fully automated tools as shown in Figure 1.4c [29, 34]. Such tools have x-, y-, and z-axis linear stages with additional tilt and rotation stages for the precise manipulation of elastomer stamps relative to the donor and receiving substrates at controllable and reproducible speeds. In this case, a composite stamp, consisting of a thin elastomer with a high-modulus backing layer, holds dimensional tolerances to avoid unwanted distortions [29]. Depending on the layouts and sizes, transfer printing rates can be up to millions of NMs per hour [13]. Registration accuracy is better than 1 μm and yields can reach nearly 100% [13]. Such tools represent an important engineering step toward machines for performing high-throughput transfer printing in industrial settings [29].

1.4
Compressive Buckling for Deterministic Assembly

1.4.1
Introduction

The traditional focus of development efforts in electronics is to increase circuit integration densities and operating speeds, to reduce the power consumption and, for display systems, to enable large-area coverage [37]. A more recent direction seeks to develop mechanically flexible and even stretchable forms of electronics

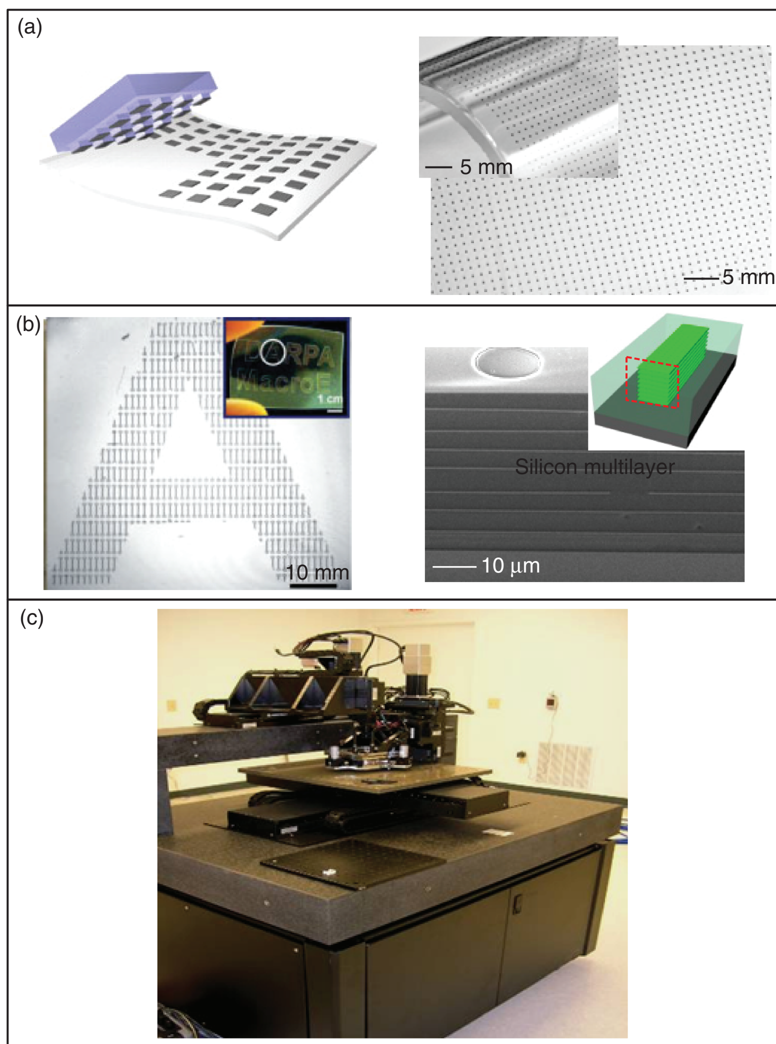

Figure 1.4 (a) Schematic illustration of transfer printing for the deterministic assembly of GaAs NMs (gray) onto a target substrate. The right frames provide optical images of GaAs NMs (small black squares) printed onto a glass substrate (main image) and a bent sheet of plastic (inset). Left frame: Reproduced from Park *et al.* [34], with permission of AAAS. Right frame: Reproduced from Rogers *et al.* [13], with permission of Nature Publishing. (b) The left panel is an optical image of printed patterned patches of silicon NMs on a PET sheet. The right panel is a cross-sectional SEM image of an eight-layer stack of silicon NMs (∼340 nm in thickness) separated by transparent layers of polymer. The inset is a schematic illustration; the cross-section shown in the main image is outlined by the red box. Left frame: Reproduced from Lee *et al.* [25], with permission of Wiley. Right frame: Reproduced from Rogers *et al.* [13], with permission of Nature Publishing. (c) Picture of a high-throughput, automated transfer-printing tool [29]. (Reproduced from Carlson *et al.* [29], with permission of Wiley.)

to allow applications that are impossible to address using conventionally hard, planar integrated circuits [38]. Examples include sensory circuits for human organs, devices with bioinspired designs (i.e., electronic eye cameras, active camouflage) and wearable communication devices. Such devices demand lightweight construction and ability to conform to complex, curvilinear substrates, or biological tissues, while maintaining high performance and reliable operation.

The synthesis and assembly techniques described in previous sections offer powerful capabilities for exploiting silicon NMs in many types of devices. NMs are naturally flexible because the bending strains and stiffnesses decrease linearly and cubically with thickness, respectively. Stretchable devices must not only be bendable but also be compatible with large strain deformations. This type of mechanics can be achieved in two conceptually different ways, either by using new materials such as graphene and carbon nanotube composites, or by using new structural layouts with existing silicon NMs [38]. The latter strategy is naturally compatible with well-developed semiconductor techniques, and represents a key advantage that follows from use of unusual structures rather than unusual materials.

Buckling, also called *wrinkling*, is ubiquitously observed in many aspects of daily life, from the aging of human skin or the dehydration of apples [39]. Buckling has historically been viewed as a mechanism for structural failure [39]. The pioneering work of Whitesides *et al.* in the late 1990s showed that this behavior can be controlled to generate interesting, well-defined, micro- and nanoscale geometries in thin metal films evaporated directly onto elastomer substrates [40]. The controlled buckling of silicon NMs on compliant substrates can form complex, three-dimensional structural layouts of utility in stretchable electronics. Such architectures of silicon NMs can provide electrical properties comparable to conventional, rigid integrated circuits made of wafer-based single-crystal silicon, while allowing stretching, folding, compressing, twisting, and other demanding modes of deformation without inducing damage or fatigue in circuit elements [37, 41–46]. The following section introduces three different strategies for using buckling phenomena to advantage: buckling on compliant substrates for wavy layouts [37, 41–44], controlled delamination buckling for wavy layouts [45], and deterministic assembly of complex, three-dimensional architectures by compressive buckling [46].

1.4.2 Buckling on Compliant Substrates for Wavy Layouts

The strategy to render silicon NMs in stretchable formats is remarkably straightforward: "wavy" layouts formed by controlled compressive buckling on compliant substrates offer stretchability with a mechanics similar to that of an accordion bellows [37]. The fabrication sequence appears in the left frames of Figure 1.5 [37]. The process starts with the generation of single-crystal silicon ribbons on SOI wafers (top panel) using the top-down, wet-etching approach described in Figure 1.1. In the next step (middle panel), a prestrained, flat elastomeric substrate

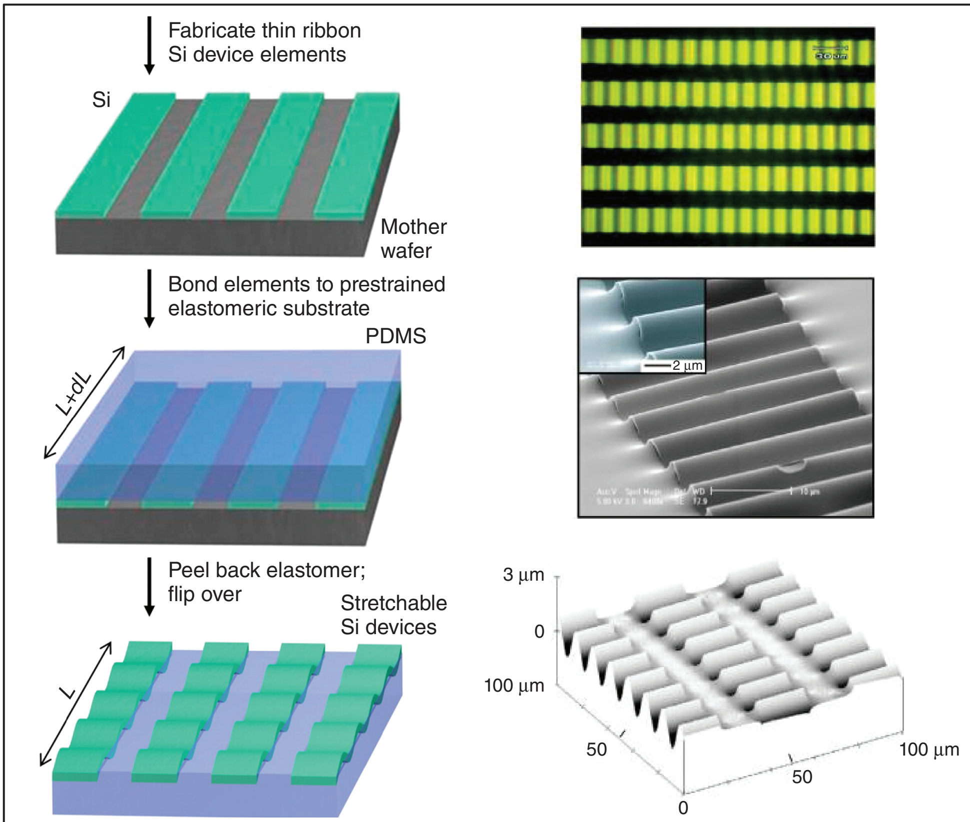

Figure 1.5 Schematic illustration of the steps involved in fabricating "wavy" silicon layouts by controlled uniaxial buckling (left frames). Optical (top), SEM (middle), and AFM (bottom) images of wavy silicon structures (right frames). Left frame: Reproduced from Khang *et al.* [37], with permission of AAAS. Right frame: Reproduced from Jiang *et al.* [42], Copyright (2007) National Academy of Sciences, U.S.A.

(1 – 3 mm thick PDMS), conformally contacts the silicon ribbons to form Si–O–Si covalent bonds by condensation reactions of surface hydroxyl groups. Peeling the PDMS away transfers the ribbons onto the surface of the PDMS substrate. Releasing the prestrain leads to compressive stresses on the silicon ribbons that generate well-defined wavy layouts on PDMS surfaces through initiation of a buckling instability (bottom panel).

The right frames in Figure 1.5 are optical (top panel), SEM (middle panel), and AFM (bottom panel) images, indicating intimate mechanical coupling between silicon and PDMS at all points at the interface [42]. Wavy layouts formed in this manner are highly sinusoidal and have excellent uniformity in amplitudes (<±5%) and wavelengths (<±3%) [42]. The resulting silicon/PDMS structures can be reversibly stretched and compressed. Mechanical modeling reveals that wavy silicon behaves mechanically as an accordion bellows and can accommodate

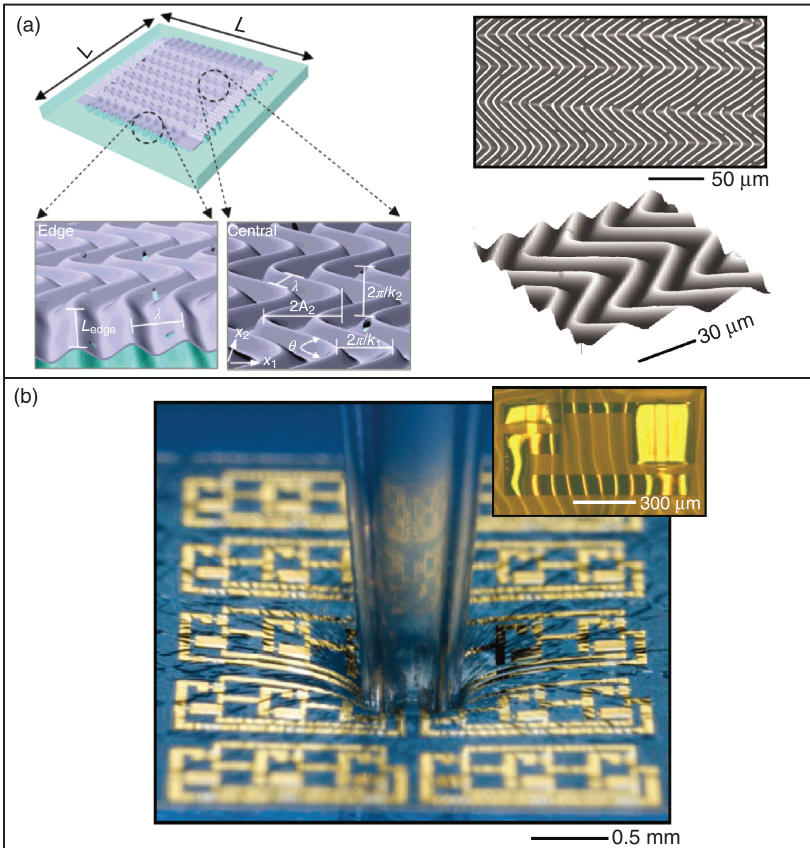

Figure 1.6 (a) Schematic illustration of controlled biaxial buckling of silicon NMs (left frames). Buckled, stretchable silicon NMs (∼100 nm in thickness) in a wavy herringbone layout bonded to an underlying PDMS substrate, presented in optical (top) and AFM (bottom) images (right frames). Left frame: Reproduced from Choi *et al.* [43], with permission of American Chemical Society. Right frame: Reproduced from Rogers *et al.* [38], with permission of AAAS. (b) Fully stretchable integrated silicon circuit in a wavy geometry, compressed at its center by a glass capillary tube (main) and wavy logic gate built with two transistors (top right inset) [38]. (Reproduced from Rogers *et al.* [38], with permission of AAAS.)

applied strains through changes in amplitudes and wavelengths [42]. As a result, the peak strains in the wavy silicon layouts can be 10–20 times smaller than the applied strains, corresponding to a stretchable mechanics that is 10–20 times higher than the intrinsic fracture limits of the silicon [37, 42].

2D wavy geometries can also be formed in silicon NMs by use of biaxially prestrained PDMS substrates as shown in left frames of Figure 1.6a [43]. Here, large NMs are released from SOI wafers with the aid of arrays of small holes to allow access of HF etchant to the buried oxide layer. Optical (top) and AFM (bottom) images of as-fabricated silicon wavy structures are in the right frames

of Figure 1.6a, demonstrating that the NMs form into waves with a herringbone configuration during the biaxial buckling process. Strains applied in any direction can be accommodated by corresponding changes in amplitudes, wavelengths, and spatial layouts of the wavy structures, with maximum strain levels at 10–20% [43].

The buckling strategies described here only depend on relatively simple, linear elastic mechanical responses, and can be applied to wide ranging classes of materials in various geometries, from inorganic nanoribbons, nanomembranes, to carbon monolayers and nanotubes [39, 44, 47–50]. Buckling has also been exploited to yield advanced, stretchable, integrated circuit systems using silicon in wavy layouts on ultrathin plastic substrates, as shown in Figure 1.6b [51]. This example includes an array of silicon transistors, logic gates, and ring oscillators. The "soft" elastic nature is demonstrated by the main image in Figure 1.6b, showing the circuit deformed in the center with a glass pipette [38]. The upper inset shows a pair of transistors in an inverter, indicating more complex wavy configurations than those simple sinusoidal and herringbone geometries in Figures 1.5 and 1.6a due to the influences of material and thickness heterogeneity. The mechanics principles are, however, similar: the wavelengths, amplitudes, and spatial layouts change to accommodate applied strains in a manner that avoids mechanical fracture of the constituent materials. Systems with this design represent realistic and scalable pathways to stretchable electronics by the approach of controlled compressive buckling [38].

1.4.3 Patterned Adhesion for Controlled, Large-Scale Buckling

A limitation of the strategy outlined in Figures 1.5 and 1.6 is that the patterns of buckling arise spontaneously, as dictated by the underlying physics, and the materials and circuit layouts; they are often nonoptimal for achieving high stretchability. Introduction of lithographically patterned surface chemistry into the overall process flow enables precise spatial control over adhesion sites on either PDMS or silicon surfaces. The result is an ability to engineer the buckling geometries to advantage in the overall stretchability [45]. Periodic or aperiodic wavy configurations can be created with deterministic control over the entire geometries of the silicon NMs [45].

Figure 1.7a (left frame) illustrates the fabrication process [45]. To begin with, PDMS substrates are selectively oxidized in lithographically patterned areas by UV/ozone exposure or oxygen plasma treatment. These treatments cover the PDMS surface with hydroxyl termination by removing methyl groups, thereby enabling interfacial chemical reactions between PDMS and silicon to form Si–O–Si bonds. Relaxing the prestrain leads to the formation of buckled wavy structures that, at sufficient levels of prestrain, involves complete delamination of the silicon from untreated, native PDMS surfaces where the adhesion is due only to van der Waals interactions. The SEM image in Figure 1.7a (right) shows buckled silicon nanoribbons in wave structures (~290 nm in thickness, ~50 μm in width), formed on a PDMS substrate patterned to yield variations of

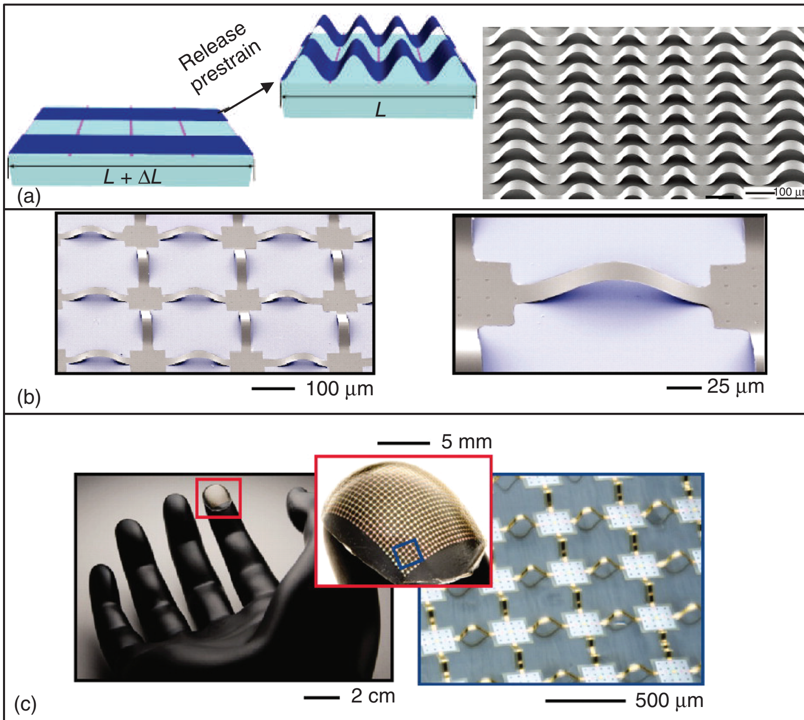

Figure 1.7 (a) Schematic illustration for delamination buckling of silicon on an elastomeric substrate with lithographically patterned surface adhesion sites (left). SEM image of the buckled silicon with variations in wavelengths and amplitudes (right). (Reproduced from Sun *et al.* [45], with permission of Nature Publishing.) (b) Moderate (left) and high-resolution (right) SEM images of silicon NMs (~100 nm in thickness) patterned into an open-mesh, arch-shaped, buckled layouts onto a rubber substrate. (Reproduced from Rogers *et al.* [38], with permission of AAAS.) (c) Stretchable silicon circuits with an open-mesh design, wrapped onto a figure tip model, demonstrated in low (left), moderate (middle), and high (right) magnification optical images. (Reproduced from Rogers *et al.* [38], with permission of AAAS.)

wavelengths and amplitudes [45]. In such layouts, the maximum tensile strain applied to the PDMS during the process (i.e., peak strain) is about 100 times larger than the intrinsic silicon fracture limit, and is significantly larger than that achieved in fully bonded wavy geometries in Figures 1.5 and 1.6 [45]. By the deposition of thin films of silicon dioxide to yield the appropriate surface chemistry, this same approach also can be used for the controlled delamination buckling of other functional materials such as GaAs [39, 41, 45]. Interestingly, the buckling amplitudes and wavelengths are approximately independent of material properties (i.e., Young's modulus and thickness), and are determined only by the spatial geometry of PDMS surface treatments and the applied prestrain [45].

The strategy described here can also be used for the deterministic assembly of open-mesh layouts on elastomer substrates for stretchable electronics, as shown

in Figure 1.7b [38]. Such buckled, arch-shaped interconnecting structures can accommodate applied strains of 100% or more [38]. An advanced circuit example is presented in Figure 1.7c, with arc-shaped cables of metal and plastic in neutral mechanical layouts and silicon devices located on the notes of the mesh. As shown in Figure 1.7c, this circuit system, which includes 1404 silicon vias and 702 metal lines, can be conformally integrated onto a fingertip model, providing clear evidence of the scalability of these approaches to active stretchable electronics for various applications [52].

1.4.4
Deterministic Assembly of Complex, Three-Dimensional Architectures by Compressive Buckling

Complex, 3D architectures appear in all biological systems, providing sophisticated, essential functions in even the most basic forms of life [53–55]. Inspired by biological systems, 3D mesostructures of functional materials have broad envisioned applications from biomedical devices to microelectromechanical components, metamaterials, sensors, electronics, and others [46, 56–59]. Existing approaches such as volumetric optical exposures [60], colloidal self-assembly [61], residual stress-induced bending [36], and template growth [62] have achieved great success in making certain class of 3D structures using selective functional materials, but with various key limitations. Extensions of the controlled buckling strategies described in Figures 1.5–1.7 can create additional design opportunities, through compression-induced assembly of micro/nanostructured silicon NMs on elastomeric substrates. The process involves geometric transformation of lithographically fabricated 2D silicon NM precursors into sophisticated, 3D layouts [46]. The process begins with the micro/nanofabrication of 2D silicon precursors on SOI wafers using the strategy described in Figure 1.1. In the next step, precisely controlled bonding sites are created at strategic locations by lithographically defined exposure to UV ozone for the formation of surface hydroxyl termination (red dots in Figures 1.8a–c). A soft silicone substrate, which serves as a platform for deterministic assembly, is uniaxially or biaxially stretched to a large level of prestrain and exposed to UV ozone to generate spatially uniform hydroxyl groups. Transfer printing (Figure 1.2) allows retrieval of 2D silicon precursors from SOI wafers and their delivery onto prestrained silicone surfaces, leading to strong, spatially selective bonding (work of adhesion $>8\,J/m^2$) via covalent linkages due to condensation reactions at the regions of silicon with hydroxyl groups [46]. By contrast, weak van der Waals forces dominate interfacial adhesions at all other locations (work of adhesion $\sim0.2\,J/m^2$) [46]. Relaxing the silicone substrates induces large compressive forces on 2D silicon precursors, which lift the weakly bonded regions of 2D precursors and deform them into complex, 3D architectures by combined motions of twisting, bending, and translating. Buckled 3D layouts of silicon NMs are governed by (i) the 2D layouts of silicon precursors, (ii) the strategic locations of bonding sites, and (iii) the nature and magnitude of the prestrain in the assembly platform.

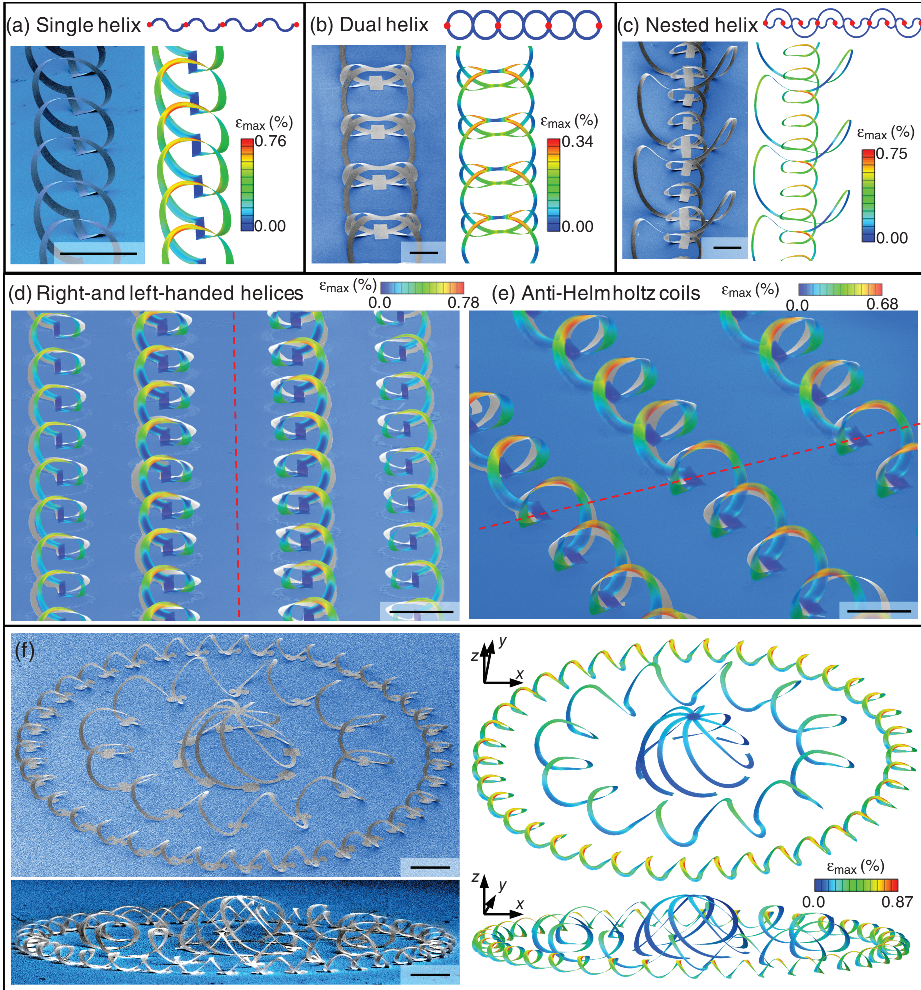

Figure 1.8 (a) Schematic illustration of a 2D silicon precursor with bonding sites (red; top), SEM image of a single helical coil formed from this precursor (left), and corresponding FEA prediction (right). Similar results for a double helical coil (b), and a nested, coaxial pair of connected helical coils (c). (d) SEM image with overlaid FEA prediction of helical coils with right- and left-handed chirality, on the left and right sides of the dashed red line, respectively. (e) SEM image with overlaid FEA prediction of structures whose chirality changes abruptly at the location defined by the dashed red line. (f) SEM images and FEA prediction of a complex 3D mesostructure formed from a 2D precursor that consists of closed-loop circular filamentary serpentines and radially oriented ribbons, selectively bonded to a biaxially stretched silicone substrate. In all cases, the color in the FEA results corresponds to the maximum principal strains. The scale bars in all images are 400 μm. (Reproduced from Xu *et al.* [46], with permission of AAAS.)

Figure 1.8a highlights a simple case: a uniform, single helical coil buckled from a 2D silicon serpentine ribbon (2 μm thick, 50 wide) starting with a uniaxial prestrain of ~90%. Experimental results (the left SEM image) are in quantitative agreement with finite element analyses (FEA) with the relative differences below 8.5%. Modifying the patterns of the 2D precursors and the distributions of bonding sites allows access to dual helices (Figure 1.8b), nested architectures (Figure 1.8c), helices with different chirality (Figure 1.8d), and even helices with abrupt changes of chirality at selected locations (Figure 1.8e). A complex, 3D silicon mesostructure, consisting of a concentric pair of toroids and a separate hemispherical "cage" appears in Figure 1.8f. This structure follows from closed-form circular 2D silicon precursors on equal-biaxially stretched assembly platforms. The remarkably good agreement between experimental results and FEA prediction further demonstrates that this strategy represents a deterministic route for making 3D silicon mesostructures with high fidelity and accuracy. In all examples of Figure 1.8, the peak strains (from ~0.34% to 0.90%) occur at locations of large changes in curvature, less than the intrinsic strain limit of silicon (~1%).

Repeating, mixing, and nesting some basic building blocks can yield large-scale, interconnected 3D mesoscale networks as shown in Figures 1.9a,b. Figure 1.9a shows an 8 × 8 array of the double-floor helix structure that consists of eight evenly spaced helices on the first floor, and another eight helices, with the axial direction

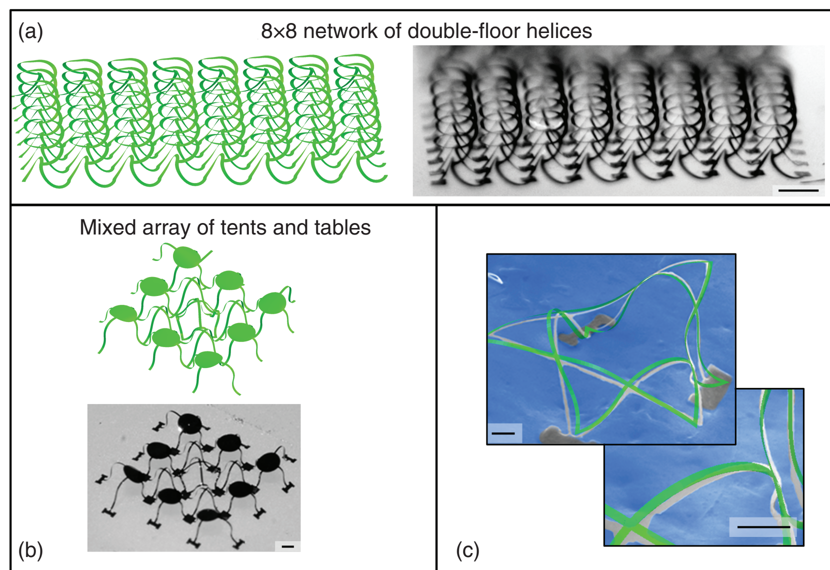

Figure 1.9 (a) Distributed 3D mesoscale network comprising an 8 × 8 network of double-floor helices, FEA predication (left) and optical image (right). (b) 3D mesostructures composed of a mixed array of tents and tables. The scale bars in (a) and (b) are 400 μm. (c) 3D mesostructures of silicon with lateral dimensions and thicknesses in the submicron regime, with overlaid FEA predictions. The scale bars in (c) are 5 μm. (Reproduced from Xu *et al.* [46], with permission of AAAS.)

rotated by 90° on the second floor. The example in Figure 1.9b corresponds to a mixed array consisting of four regular table structures, four tilted tables, four tents, and one double-floor tent at the center. Submicron features are also possible, as demonstrated in a "starfish" framework that incorporates silicon ribbons with widths of 800 nm and thicknesses of 100 nm (Figure 1.9c). This same assembly approach can also be used in additional classes of materials, such as metals (e.g., nickel), dielectrics (e.g., polyimide and epoxy), and patterned combinations of these, in single crystalline, polycrystalline, and amorphous forms [46].

1.5 Functional Devices Made from Silicon Nanomembranes

Silicon NMs open up device opportunities that would be unachievable with conventional semiconductor technologies. Dissolution of ultrathin silicon in biofluids leads to the idea of "transient electronics," where implanted devices are completely resorbable by the body after a service period to avoid the need for surgical retrieval [63–65]. Mechanical flexibility in silicon NMs, combined with transfer printing and compressive buckling strategies, enables integration with biological systems in an intimate and noninvasive way [66–68]. Examples include electronic systems assembled on thin, elastomeric sheets that establish conformal contact with the uneven surfaces of organs, such as the skin, heart, and brain, to perform precise spatiotemporal measurements [66–68]. When downsized to the dimensions of individual cells, these semiconductor devices can be implanted in the vicinity of the cells to realize close-range cellular stimuli and monitoring [69]. Furthermore, bending, stretching of silicon NM-based building blocks to form nonplanar geometries can be exploited in devising bioinspired devices, such as arthropod eye cameras and artificial camouflage skins [70, 71]. The following sections describe examples of such unusual systems in some detail.

1.5.1 Physically Transient Electronics

The stable, long-lived operation of modern electronics becomes a drawback when one considers implantable biomedical devices that need to function only during a transient body process such as wound healing. Retrieval of conventional electronic implants would require surgical intervention, which not only delays patient recovery, but also poses additional risks. One solution is to take advantage of the ability of silicon NMs to dissolve by hydrolysis in biofluids, and use them to build completely soluble electronic circuits on silk substrates with metals such as Mg, Fe, Zn, and dielectrics such as MgO and SiO_2 [63–65].

Figure 1.10a presents a simple prototype of a physically transient circuit of this type [63]. This example includes various electronic components such as inductors, transistors, capacitors, and so on, formed on a silk substrate. Fabrication exploits transfer printing of doped silicon NMs as semiconductors,

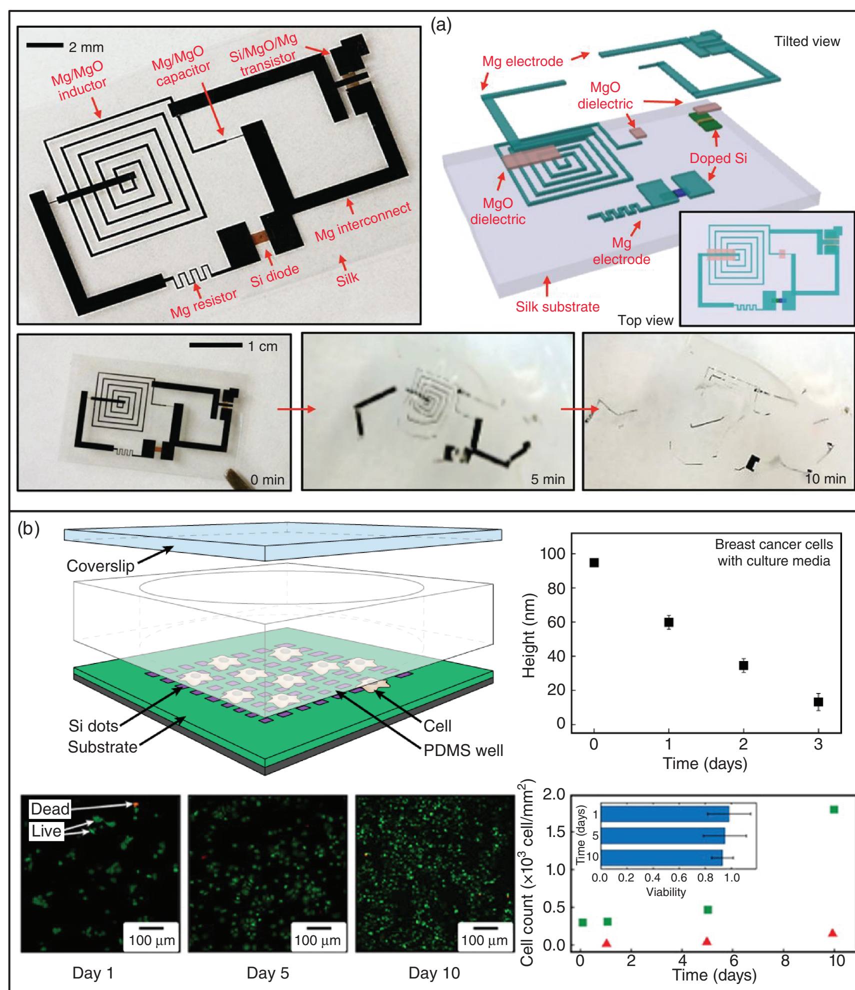

Figure 1.10 (a) Image of a transient electronic system that incorporates inductors, capacitors, resistors, diodes, transistors, and interconnects all on a silk substrate (top left). Tilted exploded view of the device showing structures of individual components (top right). The inset shows the top view of the overall device. The bottom frames show the time sequence of the dissolution in DI water. (Reproduced from Hwang *et al.* [63], with permission of AAAS.) (b) Exploded view of an experimental setting to study the *in vitro* cytotoxicity and dissolution of silicon NMs (top left). Plot of average height of silicon NMs as a function of elapsed time, showing the constant dissolution of silicon (top right). Fluorescent images of stained cells after 1, 5, and 10 days of culturing used for live and dead cell counts (bottom left). Plot of live (green squares) and dead (red triangles) cell counts as a function of elapsed time showing the growth of population (bottom right). The inset shows a fairly consistent cell viability after 1, 5, and 10 days. (Reproduced from Hwang *et al.* [65], with permission of American Chemical Society.)

patterned physical vapor deposition of Mg, MgO, and SiO_2 as electrical contacts and dielectrics, respectively, and solution-casting of silk as the global substrate. Assembling individual parts and applying ultrathin Ti layers to selective regions as adhesion promoters completes the fabrication. The NM geometries of the silicon and the thin film nature of the other layers are crucial in this context because they improve solubility by shrinking material dimensions and maximizing area-to-volume ratios. At the same time, these same features offer mechanics that favor integration onto biodegradable, elastomeric substrates, which in turn creates a system with sufficient flexibility to make intimate contact with the body. In this example, the silk disintegrates after full immersion in deionized water for ∼15 min (bottom panels of Figure 1.10a). The dissolution time can be tuned (from couple of seconds up to several months) by adjusting the properties of the substrate and encapsulation layers, thereby expanding the versatility of transient electronics from short-term, diagnostic uses to long-term, monitoring purposes [63].

Biocompatibility of transient electronics represents a critically important consideration for all biomedical applications [65]. *In vitro* evaluations of the cytotoxicity and dissolution use an experimental setup shown in Figure 1.10b. Metastatic breast cancer cells cultured on a substrate with an array of silicon NMs allow rapid evaluation. The average height of the silicon NMs can be measured as a function of the elapsed time (top right panel of Figure 1.10b). Fluorescent images of stained cells (bottom left panel of Figure 1.10b) allow determination of live and dead cell counts (bottom right panel of Figure 1.10b). The data clearly indicate cell viability during and after the consumption of silicon NMs, indicating a lack of any measurable toxicity [65].

1.5.2
Injectable, Cellular-Scale Optoelectronic Devices for the Brain

Optogenetics is a relatively recent technique in neuroscience research that exploits light to control neural activity. In the conventional embodiment of this method, fiber-optic probes that pierce into the depth of the brain deliver light pulses for stimulation/inhibition. External systems provide the light source, the power supply, and control. The fiber optic tether not only constrains the mobility of the animal subjects of optogenetics studies, but also increases the likelihood for undesirable tissue lesion, irritation, and immune response. A silicon NM-based optogenetic device design, as shown in Figure 1.11, can avoid these drawbacks [69].

Figure 1.11a displays the layout of devices that consists of arrays of GaN microscale inorganic light-emitting diodes (μ-ILEDs) sandwiched between microscale inorganic photodiodes (μ-IPDs) built using Si NMs, thermal and electrophysiological sensors, and actuators [69]. These components mount on a ∼20 μm thick microneedle to facilitate penetration into the brain. Here, the device and the microneedle adhere together with purified silk fibroin, which is bioresorbable upon contact with cerebrospinal fluid, thereby releasing the device

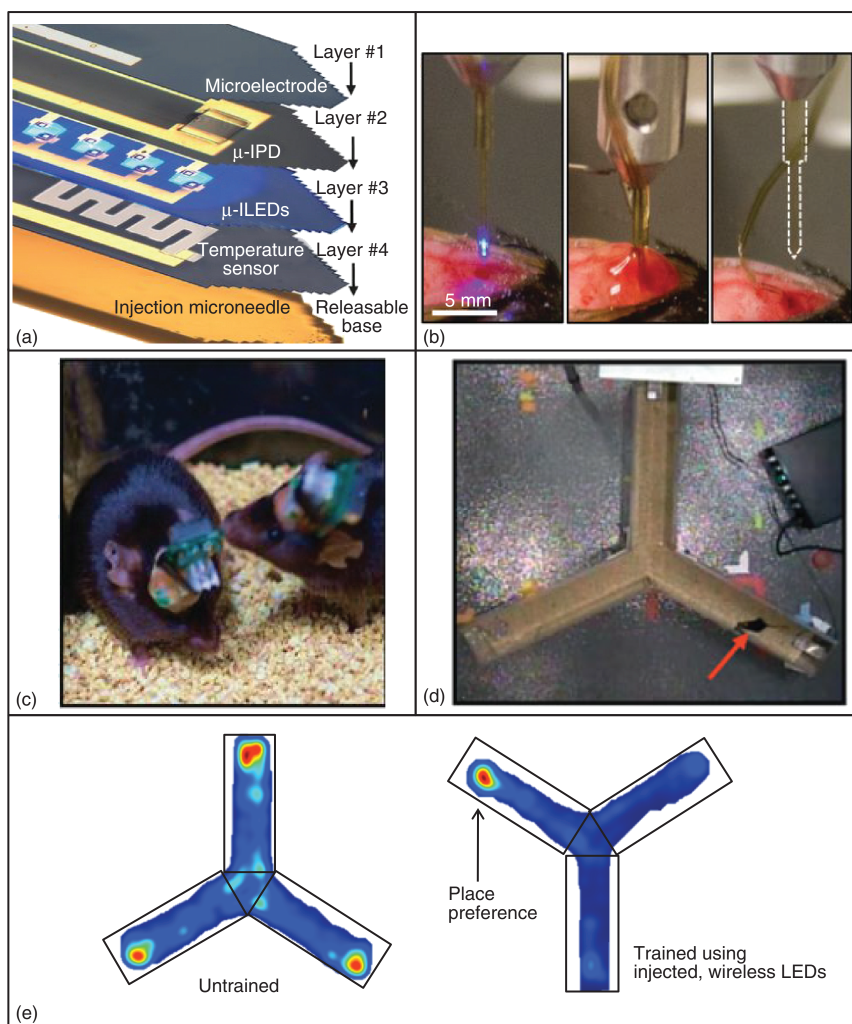

Figure 1.11 (a) Exploded view of an injectable optoelectronic device. From top to bottom: a Pt microelectrode for electrophysiological measurements, a silicon μ-IPD for optical measurements, a μ-ILED array for optical stimulation, and a Pt serpentine wire for temperature measurements and thermal stimulations. The system is mounted on a microneedle for injection. (b) Process of device injection. Cerebrospinal fluid dissolves the binding silk fibroin, releasing the device from microneedle. (c) Photograph of freely moving mice wearing lightweight, flexible wireless modules. (d) Y-maze setup to study the effectiveness of the device. The red arrow indicates the presence of a mouse wearing the device. (e) Heat map of activity showing the absence of location preference in untrained mice (left frame). Map showing the development of robust location preference of trained mice by optical stimulation (right frame). Panel (d): Reproduced from Rogers [66], with permission of MRS. Panels (a), (c), and (e): Reproduced from Kim *et al.* [69], with permission of AAAS.

(Figure 1.11b). The exposed end of the device electrically connects to a lightweight (~2.0 g), miniaturized wireless powering module. This construct allows natural motion, without tether constraints, as is evident in Figure 1.11c [69]. A notable additional advantage is the capability for delivering light in the direct vicinity of targeted neurons, while causing negligible local temperature rise. Other features include extreme mechanical compliance and minimal volume to reduce adverse effects of implantation, such as neuronal loss, gliosis, and immune responses [69].

The effectiveness of the device can be demonstrated in classical optogenetics studies, which involve mice in a Y-shaped maze (Figures 1.11d,e). Here, the mice are free to explore the maze, but receive wirelessly controlled light exposure from the implanted μ-LEDs only when they enter the bottom right corner. Upon optical stimulation, dopaminergic neurons that include a channel rhodopsin (a protein which provides light-activated ions) generate salient stimuli sufficient for behavioral conditioning. As a result, trained mice develop a locational preference after 5 days of exposure, absent any physical reward; the untrained mice, on the other hand, exhibit no such preference (Figure 1.11e).

1.5.3 Three-Dimensional Integumentary Membranes for Spatiotemporal Cardiac Measurements

An interesting area of application for stretchable electronics is in conformal integration with human organs for physiological measurements. For cardiac mapping, an ideal strategy involves wrapping the heart with an "electronic membrane" that includes various sensors, to perform 3D, close-range measurements. Such an integumentary circuit can be realized using the design depicted in Figure 1.12a [67]. Semiconductor sensors with various relevant functionalities can be constructed using standard planar fabrication processing, and then subsequently transferred onto a thin elastomeric substrate. Attaching this sheet onto a solid replica of the heart, followed by casting and curing of another silicone elastomeric layer and carefully peeling the layers off the replica renders the final 3D device system.

Figure 1.12b shows various components, including gold electrodes for electrocardiography (ECG) and stimulation, silicon NM strain gauges for monitoring the motion of the heart, InGaN μ-ILEDs for optical mapping, iridium oxide pads for pH detection, and gold serpentine resistors for thermal sensing and stimulation. Each component works independently and in a complementary fashion to yield complete information about the heart [67].

Due to its conformal integration with entire epicardial surface, this type of integumentary circuit enables 3D, spatiotemporal mapping of various parameters that are otherwise expensive or cumbersome to determine with conventional cardiac measuring techniques. 3D electrophysiological mapping of the heart can be constructed using electrical signals recorded by the gold electrodes, as shown in Figure 1.12c. Incorporating a variety of sensors also greatly expands the functionality of the device. For instance, pH mapping provides key information

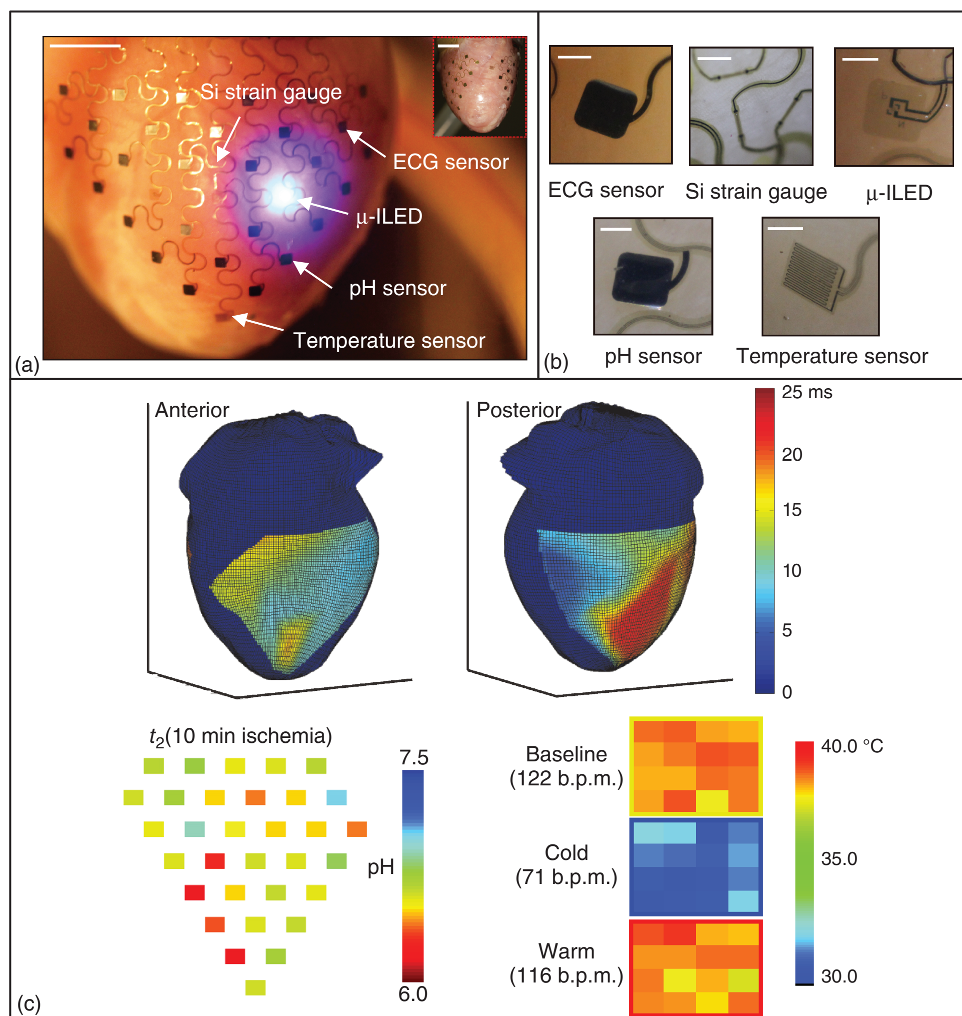

Figure 1.12 (a) Anterior view of a device mounted on a rabbit heart showing various functional components. The inset shows the posterior view. The scale bars are 6 mm. (b) Enlarged views of the metrical components. The scale bars are 500 μm. (c) Various mapping results of key cardiac parameters. Top-left and top-right: a 3D map of the heart derived from electrical signals. Bottom-left: a 2D pH map of the heart after 10 min of no-flow ischemia. Bottom right: 2D temperature monitoring of the heart during cold perfusion and subsequent recovery. (Reproduced from Xu *et al.* [67], with permission of Nature Publishing.)

on the cardiac metabolic state, while pressure and temperature mapping help identify abnormal behaviors (Figure 1.12c). The sensors can be inverted by passing currents to enable thermal or electrical stimulation for therapeutic intervention. These features define a promising clinical approach for diagnosing and treating heart diseases through the application of a noninvasive, conformal thin-sheet device [67].

1.5.4
Arthropod Eyes Inspired Digital Camera

There is long-standing interest in the development of imaging devices that resemble the eyes of arthropods, due to distinct advantages in a wide-angle field of view, infinite depth of field, low aberrations, and acute sensitivity to motion. However, the hemispherical layout of a compound eye lies outside of the realm of possibilities afforded by conventional planar semiconductor technologies. Arrays of photodetectors constructed with silicon NMs and interconnected using buckling concepts described previously can be rendered into the appropriate geometry as shown in Figure 1.13 to form a bioinspired imaging system that fully adopts a hemispherical shape [70].

For the fabrication, arrays of microlenses (made of elastomeric PDMS and supported by cylindrical posts) are precisely aligned with the photodetectors to allow optimal focusing (Figure 1.13a). Each photodetector is interconnected using serpentine metal wires for signal retrieval. To complete the camera, the assembled devices are integrated with a black matrix to eliminate the optical crosstalk (Figure 1.13b). Key requirements in the fabrication include maintaining the exact optical alignment and avoiding fracture of critical components during deformation. These outcomes are partly achieved through chemical modifications of adhesion between the optical and the electrical layers to allow selective bonding only at the locations of the microlens and photodetectors, using surface chemistries described previously. Consequently, the freely moving, serpentine metal interconnects have negligible contribution to the overall mechanics. The whole device structure then behaves mechanically much more like the PDMS used for the optical layer than like the hard materials used for the electrical layer. This response is supported by both micro-XCT and finite element modeling (FEM), where the effective modulus of the device is shown to be ~1.9 MPa, and the maximum strain can reach 50% in equibiaxial tension before fracture of the electrical components (Figure 1.13c) [70].

The camera operation involves focusing of light onto each photodetector via a corresponding microlens, with omnidirectional identical fidelity and an image resolution defined by the total number of photodetectors. Images collected at different angular directions of the camera can be combined to improve the resolution, a process adopted in arthropods through eye movements. Figure 1.13d (top) displays images of a soccer ball captured at a polar angle of −50°, 0°, and 50° relative to the camera; Figure 1.13d (bottom) shows images of a triangle and a circle placed at different distances relative to the camera. The invariant image resolution

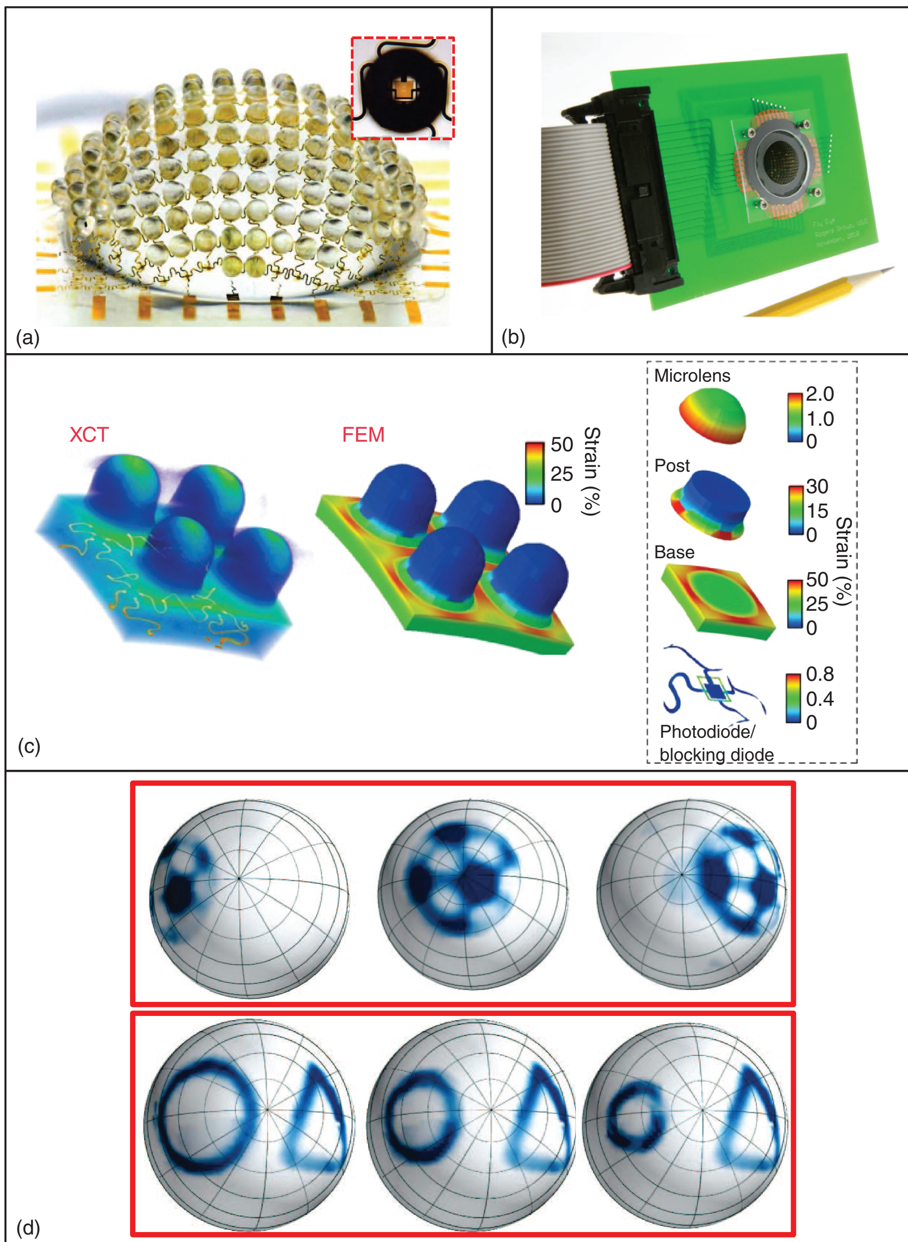
(a)
(b)
XCT
FEM
50
25
0
Strain (%)
Microlens
2.0
1.0
0
Post
30
15
0
Base
50
25
0
Strain (%)
0.8
0.4
0
Photodiode/
blocking diode
(c)
(d)

suggests wide-angle field of view and infinite depth of field [70]. Such cameras can be useful in surveillance, endoscopy, and landscape photography.

1.5.5 Cephalopod Skins Inspired Optoelectronic Camouflage Systems

The last example is related to the application of silicon NMs in adaptive camouflage systems inspired by the skins of certain cephalopods. A representative system is shown in Figure 1.14a. The top artificial chromatophore (ac) layer incorporates a matrix of microencapsulated, composite dye materials that switch between black and white when heated below and above 47 °C [71]. A highly reflective silver layer serves as an artificial leucophore (al). Subsequent layers consist of arrays of actuators and photodetectors derived from silicon NMs. The former acts as an artificial muscle (am) to enable pixelated color change in the artificial chromatophore layer through controlled Joule heating; the latter functions as an artificial opsin (ao) for light detection. The as-fabricated structure can be bent and stretched without any functional degradation (Figure 1.14b).

During operation, each photodetector senses illumination above (or below) its associated pixel, and sends electrical signals if a threshold value is exceeded. External control electronics then routes current to the co-located actuators, to heat the topmost dye pixels and induce a color change that matches, in a binary sense, the environmental brightness [71]. An experimental setup that involves a patterned background can be used to demonstrate the effectiveness of this type of artificial camouflage system. Figure 1.14c shows screenshots from a movie (extracted time in the lower right), indicating adaptive patterns subject to a continuously varying background.

1.6 Conclusions and Outlook

As outlined in this chapter, high-quality silicon NMs with precisely controlled thicknesses and lateral dimensions can be fabricated from single-crystalline

Figure 1.13 (a) Photograph of a compound, hemispherical imaging system, with the inset showing top magnified view of one pair of aligned microlens and photodetector. (b) Photograph of the completed apposition camera. (c) Micro X-ray computed tomography (XCT) and finite element modeling (FEM) results showing strain distribution after full development into hemispherical shape. The inset illustrates that maximum strains developed in critical components such as the microlens (∼2.0%) and the photodetectors (∼0.4%) are much smaller than those in the PDMS base (∼50%). (d) Pictures of a soccer ball captured at three polar angles relative to the center of the camera: −50° (left), 0° (center), and 50° (right), to illustrate the wide-angle field of view (top). Pictures of a circle and a triangle, where the circle is placed at different distances to demonstrate the infinite depth of field (bottom). Panel (c): Reproduced from Rogers [66] with permission of MRS. Panels (a), (b), and (d): Reproduced from Song *et al.* [70], with permission of Nature Publishing.

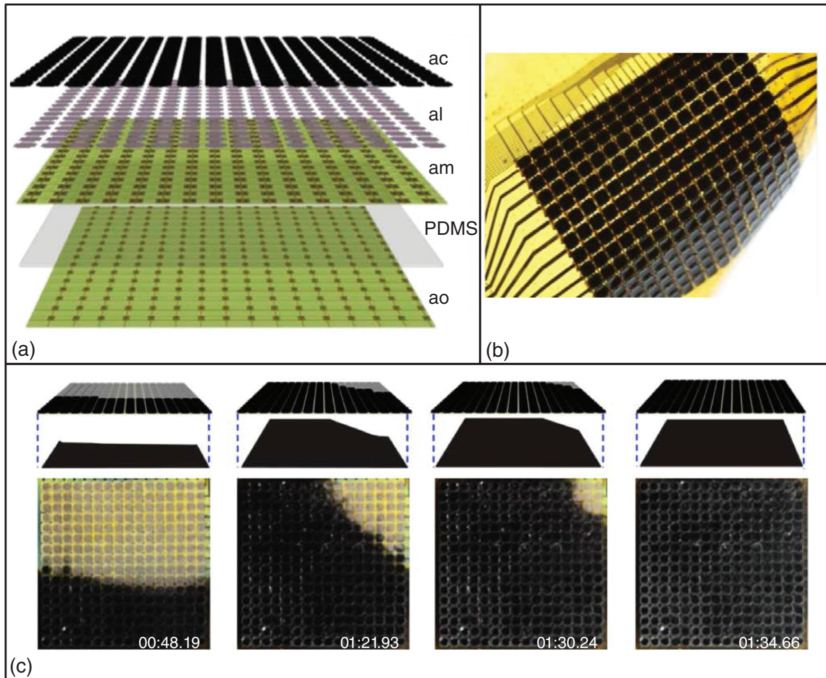

Figure 1.14 (a) Exploded view of an adaptive camouflage skin. Layer components from top to bottom are the artificial chromatophore (ac) made of microencapsulated dye, the artificial leucodye (al) made of silver deposition, the artificial muscles (am) made of silicon actuator arrays, the PDMS intermediate layer, and the artificial opsins (ao) made of silicon photodetectors. (b) Photograph of the bent and stretched device. (c) Screenshots from a movie (extracted time in the lower right) indicating adaptive patterns subject to a continuously varying background. (Reproduced from Yu *et al.* [71], Copyright (2014) National Academy of Sciences, U.S.A.)

silicon wafers in large quantities using selective or anisotropic wet-chemistry etching methods. Well-developed transfer-printing techniques can be used to nondestructively integrate micro/nano-structured NMs into advanced electronic circuits on substrates of interest, with high transfer yields and minimal levels of positional/orientational disorder. Controlled buckling strategies enable the deterministic assembly of micro/nanostructured NMs onto compliant substrates to form sophisticated, 3D architectures. Such structural designs facilitate the utility of silicon NMs in stretchable electronics by not only rivaling electrical properties of those of rigid, planar silicon-based integrated circuits, but also embodying mechanical flexibility and stretchability without damaging or fatiguing the silicon. These and other advanced synthetic and assembly concepts for silicon NMs create new possibilities in device designs with broad societal value. A variety of silicon NM-based advanced functional device systems have been achieved, including physically transient circuits, injectable systems, and cellular-scale optoelectronic devices for the brain, 3D integumentary membranes for spatiotemporal cardiac

measurements, arthropod eye-inspired digital cameras, and artificial cephalopod skins as optoelectronic camouflage systems.

Future fundamental research efforts on silicon NMs will likely focus on the further developments of efficient and cost-effective approaches to fabricate bulk quantities of high-quality NMs with precise geometries; to stack NMs heterogeneously with well-controlled surface/interfacial properties; and to nondestructively deform NMs into unusual, stretchable 3D configurations to match biological tissues for advanced biointegrated device systems. Other basic scientific challenges are to modulate the band gap properties of NMs by engineering strain distributions, and to reveal and modify fundamental features of NMs induced by nanoscale geometries [13].

The most compelling engineering possibilities for silicon NMs include further developments in NM-based biointegratable/bioinspired circuits to address important issues in human health. The future goal lies in the realization of sophisticated electronic systems, which can wrap onto the complex surfaces of biotissues, dissolve at programmed rates in biofluids, communicate and charge wirelessly inside the human body, and provide integrated functions in living systems [13]. In addition, silicon NM-based stretchable electronics also have utility in active antennas for communications, conformal sensors for structural health monitoring of aircraft, and even perhaps for bendable and stretchable cellphones [38].

The exciting fundamental challenges and the diverse engineering topics with broad societal impacts foreshadow a promising future for this field of NMs research.

References

1. Steigerwald, M.L. and Brus, L.E. (1990) Semiconductor crystallites-a class of large molecules. *Acc. Chem. Res.*, **23**, 183–188.
2. Hebard, A.F. (1993) Buckminsterfullerene. *Annu. Rev. Mater. Sci.*, **23**, 159–191.
3. Lu, W. and Lieber, C.M. (2007) Nanoelectronics from the bottom up. *Nat. Mater.*, **6**, 841–850.
4. Xia, Y., Yang, P., Sun, Y., Wu, Y., Mayers, B., Gates, B., Yin, Y., Kim, F., and Yan, H. (2003) One-dimensional nanostructures: synthesis, characterization, and applications. *Adv. Mater.*, **15**, 353–389.
5. Terrones, M. (2003) Science and technology of the twenty-first century: synthesis, properties, and applications of carbon nanotubes. *Annu. Rev. Mater. Res.*, **33**, 419–501.
6. Novoselov, K.S. (2005) Two-dimensional atomic crystals. *Proc. Natl. Acad. Sci. U.S.A.*, **102**, 10451–10453.
7. Bae, S., Kim, H., Lee, Y., Xu, X., Park, J., Zheng, Y., Balakrishnan, J., Lei, T., Kim, H., Song, Y., Kim, Y., Kim, K.S., Özyilmaz, B., Ahn, J., Hong, B., and Iijima, S. (2010) Roll-to-roll production of 30-inch graphene films for transparent electrodes. *Nat. Nanotechnol.*, **5**, 574–578.
8. Ma, R. and Sasaki, T. (2010) Nanosheets of oxides and hydroxides: ultimate 2D charge-bearing functional crystallites. *Adv. Mater.*, **22**, 5082–5104.
9. Champness, N.R. (2014) Two-dimensional materials: crystallized creations in 2D. *Nat. Chem.*, **6**, 757–759.
10. Geim, A.K. and Grigorieva, I.V. (2013) Van der Waals heterostructures. *Nature*, **499**, 419–425.

11. Menard, E., Lee, K.J., Khang, D.Y., Nuzzo, R.G., and Rogers, J.A. (2004) A printable form of silicon for high performance thin film transistors on plastic substrates. *Appl. Phys. Lett.*, **84** (26), 5398–5400.
12. Baca, A.J., Ahn, J., Sun, Y., Meitl, A.A., Menard, E., Kim, H., Choi, W.M., Kim, D.H., Huang, Y., and Rogers, J.A. (2008) Semiconductor wires and ribbons for high-performance flexible electronics. *Angew. Chem. Int. Ed.*, **47**, 5524–5542.
13. Rogers, J.A., Lagally, M.G., and Nuzzo, R.G. (2011) Synthesis, assembly and applications of semiconductor nanomembranes. *Nature*, **477**, 45–53.
14. Cavallo, F. and Lagally, M.G. (2010) Semiconductors turn soft: inorganic nanomembranes. *Soft Matter*, **6** (3), 439–455.
15. Baca, A.J., Meitl, M.A., Ko, H.C., Mack, S., Kim, H.-S., Dong, J., Ferreira, P.M., and Rogers, J.A. (2007) Printable single-crystal silicon micro/nanoscale ribbons, platelets and bars generated from bulk wafers. *Adv. Funct. Mater.*, **17**, 3051–3062.
16. Mack, S., Meitl, M.A., Baca, A.J., Zhu, Z., and Rogers, J.A. (2006) Mechanically flexible thin-film transistors that use ultrathin ribbons of silicon derived from bulk wafers. *Appl. Phys. Lett.*, **88**, 213101.
17. Zhang, P., Tevaarwerk, E., Park, B., Savage, D.E., Celler, G.K., Knezevic, I., Evans, P.G., Eriksson, M.A., and Lagally, M.G. (2006) Electronic transport in nanometer-scale silicon-on-insulator membranes. *Nature*, **439**, 703–706.
18. Yoon, J., Jo, S., Chun, I.S., Jung, I., Kim, H.S., Meitl, M., Menard, E., Li, X., Coleman, J.J., Paik, U., and Rogers, J.A. (2010) GaAs photovoltaics and optoelectronics using releasable multilayer epitaxial assemblies. *Nature*, **465**, 329–333.
19. Moutanabbir, O. and Gosele, U. (2010) Heterogeneous integration of compound semiconductors. *Annu. Rev. Mater. Res.*, **40**, 469–500.
20. Schmidt, O.G., Deneke, C., Kiravittaya, S., Songmuang, R., Heidemeyer, H., Nakamura, Y., Gottwick, R.Z., Muller, C., and Jin-Phillipp, N.Y. (2002) Self-assembled nanoholes, lateral quantum-dot molecules, and rolled-up nanotubes. *IEEE J. Sel. Top. Quantum Electron.*, **8** (5), 1025–1034.
21. Schmidt, O.G. and Eberl, K. (2001) Nanotechnology: thin solid films roll up into nanotubes. *Nature*, **410**, 168.
22. Schmidt, O.G., Rastelli, A., Kar, S.G., Songmuang, R., Kiravittaya, S., Stoffel, M., Denker, U., Stufler, S., Zrenner, A., Grutzmacher, D., Nyugen, B.-Y., and Wennekers, P. (2004) Novel nanostructure architectures. *Physica E*, **25**, 280–287.
23. Ko, H.C., Baca, A.J., and Rogers, J.A. (2006) Bulk quantities of single-crystal silicon micro-/nanoribbons generated from bulk wafers. *Nano Lett.*, **6** (10), 2318–2324.
24. Meitl, M.A., Zhu, Z., Kumar, V., Lee, K.J., Feng, X., Huang, Y., Adesida, I., Nuzzo, R.G., and Rogers, J.A. (2006) Transfer printing by kinetic control of adhesion to an elastomeric stamp. *Nat. Mater.*, **5**, 33–38.
25. Lee, K.J., Motala, M. .J., Meitl, M.A., Childs, W. .R., Menard, E., Shim, A.K., Rogers, J.A., and Nuzzo, R.G. (2005) Large-area, selective transfer of microstructured silicon: a printing-based approach to high performance thin film transistors supported on flexible substrates. *Adv. Mater.*, **17**, 2332–2336.
26. Kim, S., Wu, J., Carlson, A., Jin, S.H., Kovalsky, A., Glass, P., Liu, Z., Ahmed, N., Elgan, S.L., Chen, W., Ferreira, P.M., Sitti, M., Huang, Y., and Rogers, J.A. (2010) Microstructured elastomeric surfaces with reversible adhesion and examples of their use in deterministic assembly by transfer printing. *Proc. Natl. Acad. Sci. U.S.A.*, **107** (40), 17095–17100.
27. Sun, Y., Kim, H., Menard, E., Kim, S., Adesida, I., and Rogers, J.A. (2006) Printed arrays of aligned GaAs wires for flexible transistors, diodes, and circuits on plastic substrates. *Small*, **2** (11), 1330–1334.
28. Menard, E., Nuzzo, R.G., and Rogers, J.A. (2005) Bendable single crystal silicon thin film transistors formed by printing

on plastic substrates. *Appl. Phys. Lett.*, **86**, 093507.

29. Carlson, A., Bowen, A.M., Huang, Y., Nuzzo, R.G., and Rogers, J.A. (2012) Transfer printing techniques for materials assembly and micro/nanodevice fabrication. *Adv. Mater.*, **24**, 5284–5318.
30. Feng, X., Meitl, M.A., Bowen, A.M., Huang, Y., Nuzzo, R.G., and Rogers, J.A. (2007) Competing fracture in kinetically controlled transfer printing. *Langmuir*, **23** (25), 12555–12560.
31. Carlson, A., Lee, H., Wu, J., Elvikis, P., Cheng, H., Kovalsky, A., Elgan, S., Yu, Q., Ferreira, P.M., Huang, Y., Turner, K.T., and Rogers, J.A. (2011) Shear-enhanced adhesiveless transfer printing for use in deterministic materials assembly. *Appl. Phys. Lett.*, **98**, 264104.
32. Saeidpourazar, R., Li, R., Li, Y., Sangid, M.D., Lu, C., Huang, Y., Rogers, J.A., and Ferreira, P.M. (2012) Laser-driven micro-transfer placement of prefabricated microstructures. *J. Microelectromech. Syst.*, **21** (5), 1049–1058.
33. Carlson, A., Wang, S., Elvikis, P., Ferreira, P.M., Huang, Y., and Rogers, J.A. (2012) Active, programmable elastomeric surfaces with tunable adhesion for deterministic assembly by transfer printing. *Adv. Funct. Mater.*, **22**, 4476–4484.
34. Park, S., Xiong, Y., Kim, R., Elvikis, P., Meitl, M., Kim, D.H., Wu, J., Yoon, J., Yu, C., Liu, Z., Huang, Y., Hwang, K., Ferreira, P., Li, X., Choquette, K., and Rogers, J.A. (2009) Printed assemblies of inorganic light-emitting diodes for deformable and semitransparent displays. *Science*, **325**, 977–981.
35. Ahn, J., Kim, H., Lee, K., Jeon, S., Kang, S., Sun, Y., Nuzzo, R.G., and Rogers, J.A. (2006) Heterogeneous three dimensional electronics using printed semiconductor nanomaterials. *Science*, **314**, 1754–1757.
36. Li, X.L. (2008) Strain induced semiconductor nanotubes: from formation process to device applications. *J. Phys. D: Appl. Phys.*, **41**, 193001.
37. Khang, D., Jiang, H., Huang, Y., and Rogers, J.A. (2006) A stretchable form of single crystal silicon for high performance electronics on rubber substrates. *Science*, **311**, 208–212.
38. Rogers, J.A., Someya, T., and Huang, Y. (2010) Materials and mechanics for stretchable electronics. *Science*, **327**, 1603–1607.
39. Khang, D., Rogers, J.A., and Lee, H.H. (2008) Mechanical buckling: mechanics, metrology, and stretchable electronics. *Adv. Funct. Mater.*, **18**, 1–11.
40. Bowden, N., Brittain, S., Evans, A.G., Hutchinson, J.W., and Whitesides, G.M. (1998) Spontaneous formation of ordered structures in thin films of metals supported on an elastomeric polymer. *Nature*, **393**, 146–149.
41. Kim, D. and Rogers, J.A. (2008) Stretchable electronics: materials strategies and devices. *Adv. Mater.*, **20**, 4887–4892.
42. Jiang, H., Khang, D., Song, J., Sun, Y., Huang, Y., and Rogers, J.A. (2007) Finite deformation mechanics in buckled thin films on compliant supports. *Proc. Natl. Acad. Sci. U.S.A.*, **104** (40), 15607–15612.
43. Choi, W., Song, J., Khang, D., Jiang, H., Huang, Y., and Rogers, J.A. (2007) Biaxially stretchable "wavy" silicon nanomembranes. *Nano Lett.*, **7** (6), 1655–1663.
44. Sun, Y., Kumar, V., Adesida, I., and Rogers, J.A. (2006) Buckled and wavy ribbons of GaAs for high-performance electronics on elastomeric substrates. *Adv. Mater.*, **18**, 2857–2862.
45. Sun, Y., Choi, W., Jiang, H., Huang, Y., and Rogers, J.A. (2006) Controlled buckling of semiconductor nanoribbons for stretchable electronics. *Nat. Nanotechnol.*, **1**, 201–207.
46. Xu, S., Yan, Z., Jang, K., Huang, W., Fu, H., Kim, J., Wei, Z., Flavin, M., McCracken, J., Wang, R., Badea, A., Liu, Y., Xiao, D., Zhou, G., Chung, H., Cheng, H., Ren, W., Banks, A., Li, X., Paik, U., Nuzzo, R.G., Huang, Y., Zhang, Y., and Rogers, J.A. (2015) Deterministic assembly of functional micro/nanomaterials into complex, three-dimensional architectures by compressive buckling. *Science*, **347** (6218), 154–159.
47. Khang, D., Xiao, J., Kocabas, C., MacLaren, S., Banks, A., Jiang, H., Huang, Y., and Rogers, J.A. (2008) Molecular scale buckling mechanics

in individual aligned single-wall carbon nanotubes on elastomeric substrates. *Nano Lett.*, **8** (1), 124–130.

48. Ryu, S., Xiao, J., Park, W., Son, K., Huang, Y., Paik, U., and Rogers, J.A. (2009) Lateral buckling mechanics in silicon nanowires on elastomeric substrates. *Nano Lett.*, **9** (9), 3214–3219.
49. Xu, P., Kang, J., Choi, J., Suhr, J., Yu, J., Li, F., Byun, J., Kim, B., and Chou, T. (2014) Laminated ultrathin chemical vapor deposition graphene films based stretchable and transparent high-rate supercapacitor. *ACS Nano*, **8** (9), 9437–9445.
50. Yu, C., Masarapu, C., Rong, J., Wei, B., and Jiang, H. (2009) Stretchable supercapacitors based on buckled single-walled carbon nanotube macrofilms. *Adv. Mater.*, **21**, 4793–4797.
51. Kim, D., Ahn, J., Choi, W., Kim, H., Kim, T., Song, J., Huang, Y., Liu, Z., Lu, C., and Rogers, J.A. (2008) Stretchable and foldable silicon integrated circuits. *Science*, **320**, 507–511.
52. Ko, H., Shin, G., Wang, S., Stoykovich, M.P., Lee, J., Kim, D., Ha, J., Huang, Y., Hwang, K., and Rogers, J.A. (2009) Curvilinear electronics formed using silicon membrane circuits and elastomeric transfer elements. *Small*, **5** (23), 2703–2709.
53. Gao, X. and Jiang, L. (2004) Biophysics: water-repellent legs of water striders. *Nature*, **432**, 36.
54. Aizenberg, J., Weaver, J.M., Thanawala, M.S., Sundar, V.C., Morse, D.E., and Fratzl, P. (2005) Skeleton of *Euplectella* sp.: structural hierarchy from the nanoscale to the macroscale. *Science*, **309**, 275–278.
55. Weaver, J.C., Aizenberg, J., Fantner, G.E., Kisailus, D., Woesz, A., Allen, P., Fields, K., Porter, M.J., Zok, F.W., Hansma, P.K., and Morse, D.E. (2007) Hierarchical assembly of the siliceous skeletal lattice of the hexactinellid sponge *Euplectella aspergillum*. *J. Struct. Biol.*, **158** (1), 93–106.
56. Tian, B., Liu, J., Dvir, T., Jin, L., Tsui, J.H., Qing, H., Suo, Z., Langer, R., Kohane, D.S., and Liber, C.M. (2012) Macroporous nanowire nanoelectronic scaffolds for synthetic tissues. *Nat. Mater.*, **11**, 986–994.
57. Kim, J., Hanna, J.A., Byun, M., Santangelo, C.D., and Hayward, R.C. (2012) Designing responsive buckled surfaces by halftone gel lithography. *Science*, **335**, 1201–1205.
58. Babaee, S., Shim, J., Weaver, J.M., Chen, E.R., Patel, N., and Bertoldi, K. (2013) 3D soft metamaterials with negative Poisson's ratio. *Adv. Mater.*, **25**, 5044–5049.
59. Penmatsa, V., Kim, T., Beidaghi, M., Kawarada, H., Gu, L., Wang, Z., and Wang, C. (2012) Three-dimensional graphene nanosheet encrusted carbon micropillar arrays for electrochemical sensing. *Nanoscale*, **4**, 3673–3678.
60. Jang, D., Meza, L.R., Greer, F., and Greer, J.R. (2013) Fabrication and deformation of three-dimensional hollow ceramic nanostructures. *Nat. Mater.*, **12**, 893–898.
61. Chen, Q., Bae, S.C., and Granick, S. (2011) Directed self-assembly of a colloidal kagome lattice. *Nature*, **469**, 381–384.
62. Chen, Z., Ren, W., Gao, L., Liu, B., Pei, S., and Cheng, H.M. (2011) Three-dimensional flexible and conductive interconnected graphene networks grown by chemical vapour deposition. *Nat. Mater.*, **10**, 424–428.
63. Hwang, S., Tao, H., Kim, D., Cheng, H., Song, J., Rill, E., Brenckle, M.A., Panilaitis, B., Won, S., Kim, Y., Song, Y., Yu, K., Ameen, A., Li, R., Su, Y., Yang, M., Kaplan, D.L., Zakin, M.R., Slepian, M.J., Huang, Y., Omenetto, F.G., and Rogers, J.A. (2012) A physically transient form of silicon electronics. *Science*, **337**, 1640–1644.
64. Hwang, S., Song, J., Huang, X., Cheng, H., Kang, S., Kim, B., Kim, J., Yu, S., Huang, Y., and Rogers, J.A. (2014) High performance biodegradable/transient electronics on biodegradable polymers. *Adv. Mater.*, **26** (23), 3905–3911.
65. Hwang, S., Park, G., Edwards, C., Corbin, E.A., Kang, S., Cheng, H., Song, J., Kim, J., Yu, S., Ng, J., Lee, J., Kim, J., Yee, C., Bhaduri, B., Su, Y., Omennetto, F.G., Huang, Y., Bashir, R., Goddard, L., Popescu, G., Lee, K., and Rogers, J.A.

(2014) Dissolution chemistry and biocompatibility of single-crystalline silicon nanomembranes and associated materials for transient electronics. *ACS Nano*, **8** (6), 5843–5851.

66. Rogers, J.A. (2014) Materials for semiconductor devices that can bend, fold, twist, and stretch. *MRS Bull.*, **39**, 549–556.
67. Xu, L., Gutbrod, S.R., Bonifas, A.P., Su, Y., Sulkin, M.S., Lu, N., Chung, H.J., Jang, K., Liu, Z., Ying, M., Lu, C., Webb, C., Kim, J., Laughner, J.I., Cheng, H., Liu, Y., Ameen, A., Jeong, J., Kim, G., Huang, Y., Efimov, I.R., and Rogers, J.A. (2014) 3D multifunctional integumentary membranes for spatiotemporal cardiac measurements and stimulation across the entire epicardium. *Nat. Commun.*, **5**, 3329.
68. Xu, S., Zhang, Y., Jia, L., Mathewson, K.E., Jang, K., Kim, J., Fu, H., Huang, X., Chava, P., Wang, R., Bhole, S., Wang, L., Na, Y., Guan, Y., Flavin, M., Han, Z., Huang, Y., and Rogers, J.A. (2014) Soft microfluidic assemblies of sensors, circuits, and radios for the skin. *Science*, **344**, 70–74.
69. Kim, T., McCall, J.G., Jung, Y., Huang, X., Siuda, E.R., Li, H., Song, J., Song, Y., Pao, H., Kim, R., Lu, C., Lee, S., Song, S., Shin, G., AlHasani, R., Kim, S., Tan, M., Huang, Y., Omenetto, F.G., Rogers, J.A., and Bruchas, M.R. (2013) Injectable, cellular-scale optoelectronics with applications for wireless optogenetics. *Science*, **340**, 211–216.
70. Song, Y., Xie, Y., Malyarchuk, V., Xiao, J., Jung, I., Choi, K., Liu, Z., Park, H., Lu, C., Kim, R., Li, R., Crozier, K.B., Huang, Y., and Rogers, J.A. (2013) Digital cameras with designs inspired by the arthropod eye. *Nature*, **497**, 95–99.
71. Yu, C., Li, Y., Zhang, X., Huang, X., Malyarchuk, V., Wang, S., Shi, Y., Gao, L., Su, Y., Zhang, Y., Xu, H., Hanlon, R.T., Huang, Y., and Rogers, J.A. (2014) Adaptive optoelectronic camouflage systems with designs inspired by cephalopod skins. *Proc. Natl. Acad. Sci. U.S.A.*, **111** (36), 12998–13003.